JOURNAL OF MATERIALS SCIENCE **39** (2004) 3593–3604

A dislocation dynamics study of strength differential in particle-containing metals during cyclic loading

R. W. LEGER, T. A. KHRAISHI, Y.-L. SHEN*
Department of Mechanical Engineering, University of New Mexico, Albuquerque, NM 87131, USA
E-mail: shenyl@me.unm.edu

Dislocation dynamics simulations were carried out to study the cyclic stress-strain response of crystals containing misfit particles. The strength differential, manifested by the difference in the magnitudes of tensile and compressive flow strength during continuous loading, is examined. The computational model consists of a spherical particle and a single Frank-Read source in a specified slip plane inside a face-centered-cubic crystal. Attention is devoted to the dislocation glide behavior affected by the misfit elastic field, even when the slip plane does not intersect the particle. The multiplication of dislocation from the single source, the formation of pile-up loops as well as the unraveling of the loops upon reversed loading were all captured by the simulation. It was observed that the existence of a misfit particle gives rise to strength differential, a phenomenon of fundamentally different nature with regard to the widely recognized Bauschinger effect. The "back stress" concept was employed to analyze the simulation result. The effects of particle size and applied strain rate on the overall strength differential were also examined.

1. Introduction

Metals containing particles that are not penetrable by dislocations frequently display reduced yield strength during reversed loading in compression after an initial amount of tensile plastic deformation (or vice versa). This phenomenon of "strength differential" upon load reversal, termed the Bauschinger effect, has long been observed in many precipitation hardened alloys [1–4], dispersion strengthened metals [5–7], and metal matrix composites [8–10]. Prevailing theories for the Bauschinger effect are largely based on the concept of back stress, arising from dislocation pile-up in the form of Orowan loops or others, that aids in plastic deformation during the reversed loading phase. If one ignores the work hardening due to the interactions of mobile dislocations with solute atoms and forest dislocations, the forward yield strength (σ_y^f) of a particle-containing metal can be expressed, conceptually, as

$$\sigma_y^f = \sigma_0 + \sigma_B, \tag{1}$$

where σ_0 is the stress required to bow out the dislocations and σ_B is the back stress exerted on the matrix by the particles [11]. Upon reversed loading, the yield strength σ_y^r still consists of the contribution from σ_0, but σ_B now assists the deformation rather than opposing it. Therefore,

$$\sigma_y^r = \sigma_0 - \sigma_B. \tag{2}$$

As a consequence, the strength differential $\Delta\sigma$, defined to be

$$\Delta\sigma = \sigma_y^f - \sigma_y^r, \tag{3}$$

becomes $\Delta\sigma = 2\sigma_B$. The quantity $2\sigma_B$ characterizes the extent of permanent softening in reversed loading.

An apparent source for the back stress σ_B in the previous equations is the Orowan loops formed around the particles when the slip planes intersect the impermeable obstacles [12]. This, however, is not the sole contribution to σ_B, as will be illustrated in the present paper. We employ dislocation dynamics (DD) simulations to study the dislocation-particle interaction and its consequences under the condition that the dislocation glide path is clear of any impeding particle. The interaction arises from the particle-induced misfit elastic strain field in the metallic matrix. Such elastic field exists in almost all metals and alloys containing even incoherent precipitates or reinforcements, primarily in the form of thermal expansion mismatch strains generated during processing. The movement of dislocations

*Author to whom all correspondence should be addressed.

can be affected, resulting in sub-structures that contribute to the back stress and therefore the strength differential. It is worth pointing out that the elastic interaction considered here occurs much more frequently in materials with dilute particle concentrations than the Orowan looping events. This is because a given dislocation segment is expected to traverse the metal matrix for a relatively long distance before, if ever, approaching a particle head-on.

In this work, attention is devoted to a representative volume element containing a single spherical particle and one Frank-Read dislocation source. The overall cyclic stress-strain curves are simulated with the effects of particle size, loading direction and loading rate examined. Representative snapshots of dislocation configurations during deformation are shown. The interpretation of the back stress and particle strengthening effects within the present simulation framework and the implications in the actual Bauschinger effect found in engineering materials are also discussed.

2. Approach

2.1. Problem geometry

The computational domain, shown in Fig. 1, is a cube of side length 10,000 b, with b being the magnitude of the Burgers vector of the material, used as a measure of the length scale in this study. The x, y and z-axes are parallel to the [100], [010] and [001] directions, respectively, of the face-center-cubic (FCC) crystal; the origin is fixed at the center of the cube. A spherical particle of radius 2,000 b is located at the cube center. This is equivalent to a particle volume fraction of about 3.4%. In some calculations different radius values are used to study the effect of particle size. The initial Frank-Read source is represented by a straight dislocation, parallel to the $[\bar{1}10]$ direction with a length of $10{,}000/\sqrt{2}\,b$, lying in a (111) slip plane highlighted as a triangle in the figure. In this case the closest distance between the slip plane and the edge of the particle is 887 b. Both ends of the dislocation are fixed throughout the deformation when the dislocation experiences recurring bow-out under resolved shear stress. All three possible Burgers vectors associated with the (111) slip plane are considered in the simulation: $\frac{b}{\sqrt{2}}[10\bar{1}]$, $\frac{b}{\sqrt{2}}[0\bar{1}1]$ and $\frac{b}{\sqrt{2}}[\bar{1}10]$. The applied uniaxial loading is in the direction of [001] (z axis).

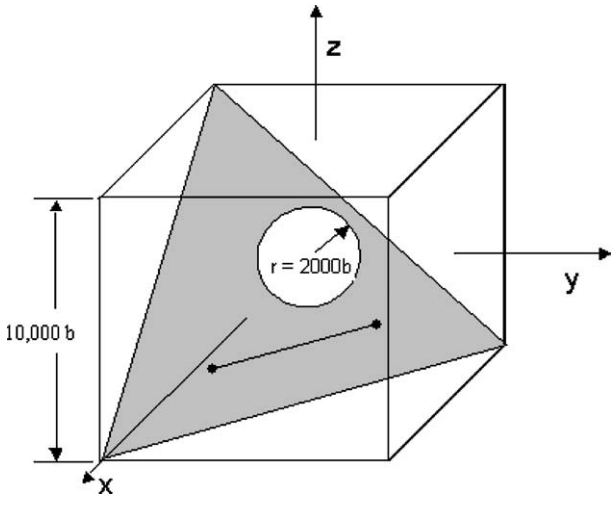

Figure 1 Schematic of the problem geometry. The x, y, z axes are in the directions of [100], [010] and [001], respectively. The origin is set at the center of the cube (and the spherical particle). The (111) slip plane containing the Frank-Read dislocation source is highlighted. The dislocation source, parallel to the $[\bar{1}10]$ direction, has two end nodes fixed at the coordinates of $x = 1667\,b$, $y = -3333\,b$, $z = -3333\,b$ and $x = -3333\,b$, $y = 1667\,b$, $z = -3333\,b$, where b is the magnitude of the Burgers vector.

2.2. Stress field due to the misfit particle

The stress field in the metal matrix imposed by the misfit particle is based on the analytical solution of a boundary value problem [13]. The problem considers an isotropic elastic spherical particle that is fitted into a smaller spherical hole in an isotropic infinite elastic medium such that the volumetric misfit is δV. The stresses generated in the matrix, expressed in terms of spherical coordinates (r, θ, ϕ), are

$$\sigma_{rr} = -\frac{4\mu_m C}{r^3}, \quad \sigma_{\theta\theta} = \sigma_{\phi\phi} = \frac{2\mu_m C}{r^3}, \tag{4}$$

where

$$C = \frac{\delta V}{4\pi\left(1 + \frac{4\mu_m}{3K_p}\right)}, \tag{5}$$

and μ and K are the shear modulus and bulk modulus, respectively; and the subscripts m and p refer to matrix and particle, respectively.

2.3. DD formulation

In recent years DD has been developed as a powerful tool by which microscale phenomena involving dislocations in crystals can be simulated [14–24]. Such simulations often are not based upon phenomenological parameters, rendering them an inherently more fundamental approach for studying plastic deformation. In three-dimensional DD simulations, continuously curved dislocation lines are approximated with a set of connected straight segments. The premise is that the self-stress of the curved dislocation, which is not explicitly known in general, can be adequately represented by the sum of the self-stresses of the discrete linear dislocation segments utilizing superposition. The self-stress of a straight dislocation segment in an infinite media [25, 26] serves as a primary ingredient incorporated into the DD code. The Peach-Koehler force of the segment i is given by

$$\vec{F}_i = \left(\underline{\sigma}_i^{\text{total}} \cdot \vec{b}_i\right) \times \vec{\xi}_i + \vec{F}_{i,\text{forward neighbor}} + \vec{F}_{i,\text{backward neighbor}}, \tag{6}$$

where $\vec{b}_i$ and $\vec{\xi}_i$ represent the Burgers vector and line sense (unit vector), respectively, of dislocation segment i. The last two force terms on the right-hand side of

Equation 6 give the self-force, arising from two nearest-neighbor segments, which acts on the segment i [19]. The term $\underline{\sigma}_{\mathrm{i}}^{\mathrm{total}}$ is the total stress tensor evaluated at the center of segment i,

$$\underline{\sigma}_{\mathrm{i}}^{\mathrm{total}} = \sum_{j=1, j\neq i}^{N} \underline{\sigma}_j + \underline{\sigma}^{\mathrm{applied}} + \underline{\sigma}^{\mathrm{particle}}, \qquad (7)$$

where the subscript j represents other dislocation segments besides i, N is the total number of segments, $\underline{\sigma}^{\mathrm{applied}}$ is the externally applied stress, and $\underline{\sigma}^{\mathrm{particle}}$ is the stress field caused by the particle, including the misfit field (given by Equations 4 and 5) and the image stress. The results presented in this paper do not include any contribution from the image stress, because incorporating image stresses in a rigorous manner is exceedingly difficult and the image stress makes only a very small contribution in the present problem. Details will be discussed in the following sections.

The results from the Peach-Koehler force calculations are used to advance the dislocation segments based on the linear mobility model,

$$\vec{v}_{\mathrm{i}}^{\mathrm{g}} = M_{\mathrm{i}}^{\mathrm{g}} \vec{F}_{\mathrm{i}}^{\mathrm{g}}, \qquad (8)$$

where $\vec{v}_{\mathrm{i}}^{\mathrm{g}}$ is the glide velocity of segment i, $M_{\mathrm{i}}^{\mathrm{g}}$ is the dislocation mobility, and $\vec{F}_{\mathrm{i}}^{\mathrm{g}}$ is the glide component of the Peach-Koehler force after subtracting out the Peierls lattice friction. The evolving dislocation structure such as bow-out, expansion/shrinkage of loops, and pile-up can thus be simulated. The macroscopic plastic strain tensor $\underline{D}^{\mathrm{p}}$ and the plastic spin $\underline{W}^{\mathrm{p}}$ are expressed as

$$\underline{D}^{\mathrm{p}} = \sum_{i=1}^{N} \frac{-l_{\mathrm{i}} v_{\mathrm{i}}^{\mathrm{g}}}{2V} (\vec{n}_{\mathrm{i}} \otimes \vec{b}_{\mathrm{i}} + \vec{b}_{\mathrm{i}} \otimes \vec{n}_{\mathrm{i}}), \quad \text{and} \qquad (9)$$

$$\underline{W}^{\mathrm{p}} = \sum_{i=1}^{N} \frac{-l_{\mathrm{i}} v_{\mathrm{i}}^{\mathrm{g}}}{2V} (\vec{n}_{\mathrm{i}} \otimes \vec{b}_{\mathrm{i}} - \vec{b}_{\mathrm{i}} \otimes \vec{n}_{\mathrm{i}}), \qquad (10)$$

where $\vec{n}_{\mathrm{i}} (= \frac{\vec{v}_{\mathrm{i}}^{\mathrm{g}}}{v_{\mathrm{i}}^{\mathrm{g}}} \times \vec{\xi}_{\mathrm{i}})$ is the unit normal vector of the slip plane for segment i, l_{i} is the segment length, and V is the volume of the simulated crystal. The stress rate is determined by the Hooke's law,

$$\dot{\underline{\sigma}} = [C^{\mathrm{e}}](\underline{D} - \underline{D}^{\mathrm{p}}), \qquad (11)$$

where $[C^{\mathrm{e}}]$ is the elastic stiffness tensor and $\underline{D}$ is the total strain rate tensor. The overall stress-strain response of the model crystal can thus be simulated.

2.4. Simulation parameters

The matrix material is single-crystal aluminum, with the magnitude of Burgers vector b equal to 0.286 nm. The dislocation mobility is taken to be 100 Pa^{-1} s^{-1} in the calculations. The base strain rate used in this work is 0.1 s^{-1}. Other magnitudes are also used for examining the effect of strain rate on the overall flow stress. The time step and dislocation segment length are mainly fixed at 10^{-9} s and 150 b, respectively. These quantities have been checked for ensuring that the solution is independent of mesh size and time step. The elastic constants of the matrix (with subscript m) and the particle (with subscript p) are $\mu_{\mathrm{m}} = 26.32$ GPa, $\nu_{\mathrm{m}} = 0.33$, $\mu_{\mathrm{p}} = 195.1$ GPa and $\nu_{\mathrm{p}} = 0.17$, where μ and ν represent shear modulus and Poisson's ratio, respectively. The bulk modulus needed for calculating the misfit stress field in Equations 4 and 5 is related to μ and ν by

$$K = \frac{2\mu(1+\nu)}{3(1-2\nu)}. \qquad (12)$$

The volumetric misfit δV caused by the particle in Equation 5 is taken to be 3% of the particle volume. This misfit is considered reasonable for aluminum alloys containing inherent intermetallic- or ceramic-based inclusions or for discontinuously reinforced aluminum containing ceramic reinforcement. The linear misfit strain induced by thermal expansion mismatch between matrix and particle during thermal excursion is expressed as

$$\Delta\varepsilon = \Delta\alpha \cdot \Delta T, \qquad (13)$$

where $\Delta\alpha$ and ΔT are the difference in coefficient of thermal expansion and temperature difference, respectively. Taking 24×10^{-6} K^{-1} and 6×10^{-6} K^{-1} as α for matrix and particle, respectively, and taking ΔT as 550 K, one obtains $\Delta\varepsilon$ of approximately 0.01 and thus the volumetric misfit strain of approximately 0.03.

It is worth pointing out that, although the matrix material in the simulation box is a single crystal, isotropic material properties are assumed because the focus here is simply to utilize the representative volume element, containing a single particle, to study fundamental micromechanical features. For the purpose of easy interpretation of results, the extent of model complexity is kept at a minimum. The use of anisotropic elasticity, as opposed to isotropic elasticity, to quantify the stress field of dislocation segments in DD simulation has been shown to result in differences, in the case of molybdenum, as high as 15% for short-range dislocation interaction [27]. However, for long-range interaction, the use of isotropic elasticity is sufficient.

3. Results

3.1. Particle induced strength differential

Fig. 2 shows the simulated overall uniaxial stress-strain response of the crystal with *no* embedded particle. The Burgers vector of the gliding dislocation is $\frac{b}{\sqrt{2}}[10\bar{1}]$. The simulation features a forward tensile loading to an applied strain of 0.0025, followed by a reversed loading back to zero strain. During forward loading, the elastic-plastic nature of the response is evident, with a plastic flow strength (defined as the maximum peak stress reached) of about 52 MPa. Upon load reversal the elastic unloading response is also evident. Subsequent compressive yielding occurs at a stress of about 52 MPa. It is clear that this reference case shows no strength differential. As mentioned in Section 2.1, two

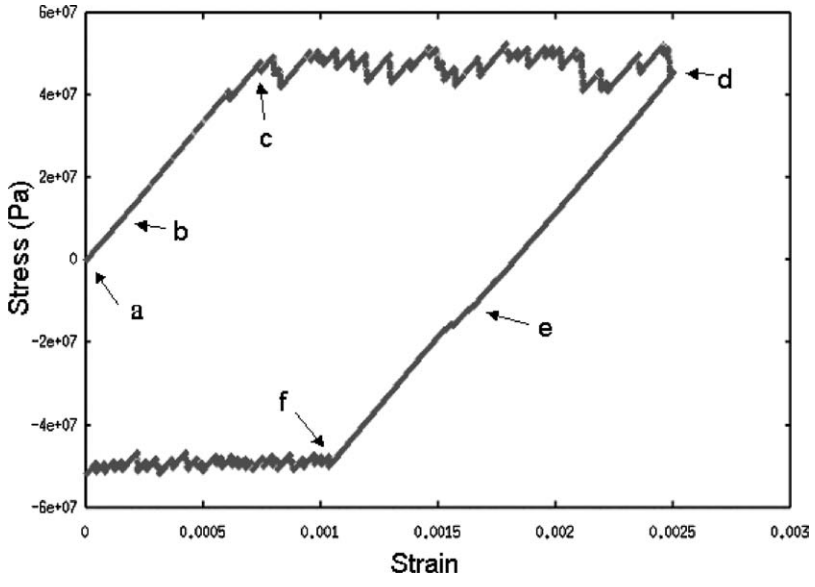

Figure 2 Simulated uniaxial stress-strain response of the crystal with no embedded particle. The Burgers vector of the gliding dislocation is $\frac{b}{\sqrt{2}}[10\,\bar{1}]$. The simulation consists of tensile loading at a constant strain rate of 0.1 s^{-1} to an applied strain of 0.0025, followed by a reversed loading at the same strain rate to zero strain.

other Burgers vectors were also considered in our calculations. The Burgers vector of $\frac{b}{\sqrt{2}}[0\bar{1}1]$ results in essentially the same stress-strain curve as in Fig. 2. In the case of $\frac{b}{\sqrt{2}}[\bar{1}10]$, however, only a linear elastic behavior can be seen because the loading does not have a resolved shear stress component in the direction of the Burgers vector. As a consequence, in the remainder of this paper simulation results based on only the Burgers vector $\frac{b}{\sqrt{2}}[10\bar{1}]$ are presented.

Fig. 3a–f show the snapshots of dislocation configurations corresponding to points a, b, c, d, e, and f labeled in Fig. 2. These views are normal to the (111) slip plane and the triangle indicates the intersection of the slip plane with the simulation box. Fig. 3a shows the initial Frank-Read source pinned at each end. Fig. 3b shows the dislocation at the beginning of tensile loading. The source is bowing out under the applied stress but the direction of bow is skewed to the left because the Burgers vector (shown in this figure) is not perpendicular to the initial dislocation line in (a). Fig. 3c shows the dislocation spiraling around the terminal point, which corresponds to the beginning of plastic flow in the crystal. The majority of the loop is outside the cubic domain so only the two end parts of the dislocation are visible here. Fig. 3d shows the configuration at the strain reversal point. Many cycles of dislocation bow-out and loop generation process have already occurred by this time. Fig. 3e shows that, upon entering the compressive regime, the dislocation bows out in the opposite direction. When the reversed yield stress is reached, Fig. 3f, the dislocation again spirals in the opposite direction about the terminal points.

Fig. 4 shows the simulated stress-strain response of the crystal containing a spherical particle of radius 2,000 b. It can be seen that the existence of the elastic misfit field causes a strong strength differential: the tensile and compressive flow stresses are approximately 94 and 36 MPa, respectively. Comparing Fig. 4 with

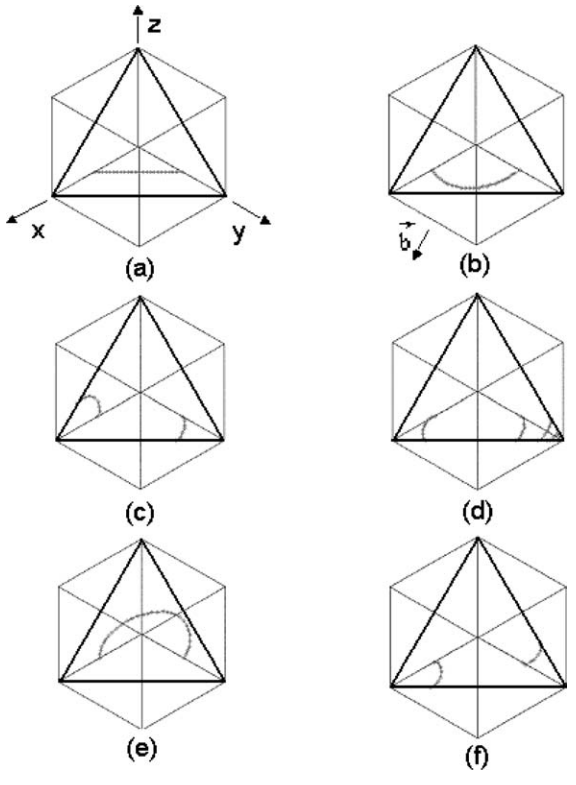

Figure 3 Dislocation configurations corresponding to points labeled on the simulated stress-strain diagram (Fig. 2) of the crystal with no embedded particle. The figure shows dislocation configurations for (a) initial Frank-Read source; (b) at the beginning of elastic deformation in tension; (c) at the beginning of plastic deformation in tension; (d) at the strain reversal point; (e) during elastic deformation in compression; and (f) at the beginning of plastic deformation in compression.

Fig. 2, the particle-bearing material shows a strengthening effect in tension but a weakening effect in subsequent compression. In Fig. 4 points a, b, c, d, e, and f are labeled along the curve; the snapshots of dislocation configuration corresponding to these stages are shown in Fig. 5a–f. For clarity the particle is removed from these figures since, in this viewing direction, the

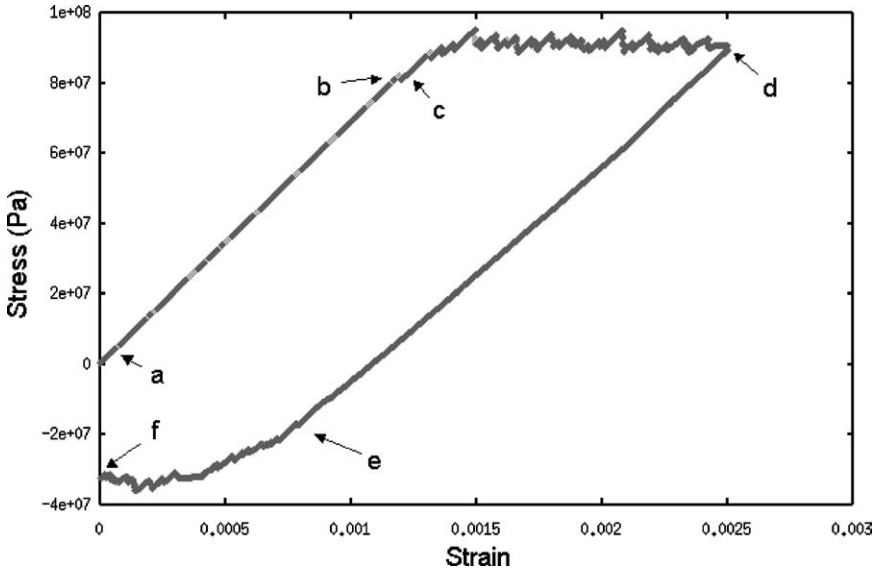

Figure 4 Simulated uniaxial stress-strain response of the crystal with an embedded particle of radius 2,000 b. The Burgers vector of the gliding dislocation is $\frac{b}{\sqrt{2}}[10\bar{1}]$. The simulation consisted of tensile loading at a constant rate of 0.1 s^{-1} to an applied strain of 0.0025, followed by a load reversal at the same strain rate back to zero strain.

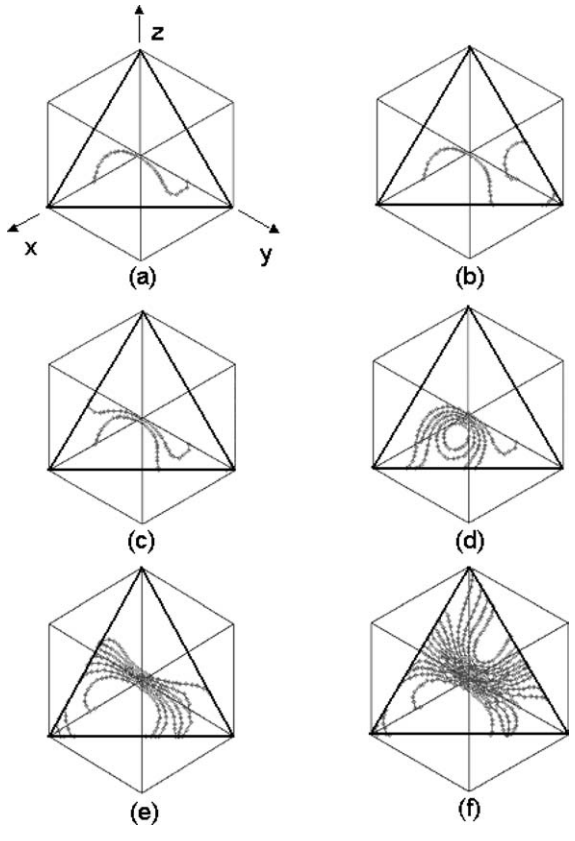

Figure 5 Dislocation configurations corresponding to points labeled on the simulated stress-strain diagram (Fig. 4) for the crystal with an embedded particle (not shown). The figure shows dislocation configurations for (a) Frank-Read source at the beginning of elastic deformation in tension; (b) at the beginning of plastic deformation in tension; (c) just after the beginning of plastic deformation in tension; (d) at the strain reversal point; (e) at the beginning of plastic deformation in compression; and (f) at the end of the loading and unloading cycle.

particle covers the underlying dislocation structure. It is observed in Fig. 5a that the dislocation configuration at the early stage of deformation is significantly different from the case with no particle. The stress field induced by the misfit particle is sufficient to activate the source and draws the dislocation upwards in the slip plane while the applied stress field is trying to pull the dislocation away in the other direction thus distorting the dislocation into an s-shape. A higher applied stress is thus needed to activate the Frank-Read mechanism than in the case with no particle, resulting in a higher elastic limit for the material. Fig. 5b shows the onset of plastic yielding. Parts of the dislocation are outside the domain. However, it is apparent that the particle-induced stress field has trapped the left portion of the dislocation. The applied stress causes the right portion to loop around the right pinning point, but, as it sweeps back, the original left portion in conjunction with the combined stress field forces it to stop and a pile-up starts to develop. This is shown in Fig. 5c. The original loop remains pinned and the second one is now operating. Similar actions repeat themselves and more loops are building up. This dislocation pile-up causes an increase in stress required to generate more new loops (i.e., to continue the plastic flow in the material). The looping action continues until the radius of the inner loop becomes too small and subsequent loop generations result in the collapse and annihilation of inner loops, thus preventing additional pile-up and resulting in a relatively constant flow stress value. The loop configuration at the load reversal point is shown in Fig. 5d. Upon load reversal the applied stress is decreased and the loops enlarge and open up. When the stress becomes compressive the dislocations are drawn in the opposite direction. Fig. 5e shows the configuration of the dislocation loops at around the reversed yield point. The outermost dislocation is nearly straight and is on the verge of bowing out in the upward direction. Dislocations start to pile up on the opposite side of the particle resulting in a buildup of loops. The configuration at the end of the load-unload cycle is shown in Fig. 5f. Although the dislocation density in this compressive phase is higher than that in the previous tensile phase, many *mobile* segments are able to

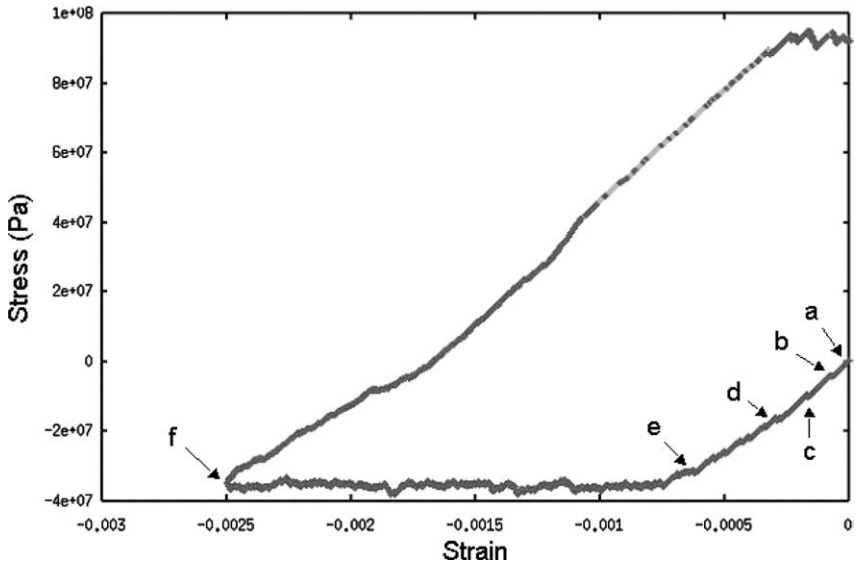

Figure 6 Simulated uniaxial stress-strain response of the crystal with an embedded particle of radius 2,000 b. The Burgers vector of the gliding dislocation is $\frac{b}{\sqrt{2}}[10\bar{1}]$. The simulation consisted of compressive loading at a constant rate of 0.1 s^{-1} to an applied strain of 0.0025, followed by a load reversal at the same strain rate back to zero strain.

sweep through the slip plane and carry the plastic flow at a lower macroscopic stress.

Although the early reversed yielding in Fig. 4 is evident, care should be taken in drawing a direct connection with the commonly conceived Bauschinger effect. This is because the current simulation results are found to be independent of the loading sequence, as presented Fig. 6 where the simulated stress-strain response is shown for the compression-first loading, followed by reversed loading into the tensile yielding regime. Here the compressive flow stress is about 38 MPa and the subsequent tensile flow stress is about 95 MPa. Apparently there is no early tensile yielding when the compression-first history is adopted. The fact that the flow stress magnitudes are approximately the same as those in the tension-first case suggests that the misfit elastic field results in a shift in the flow stress towards the tensile direction for the particular problem configuration considered, regardless of the history of the uniaxial deformation. There is, however, also a net increase in the sum of the magnitudes of tensile and compressive flow stresses compared to the particle-free case, meaning that a net strengthening effect exists.

Fig. 7a–f show the snapshots of dislocation configuration corresponding to points a, b, c, d, e and f highlighted in Fig. 6. The major difference between the configurations shown in Figs 5 and 7 are in the early configuration. It is observed in Fig. 7a that the particle induced stress and applied stress act together in this case to pull the dislocation upward. From Fig. 7b to d, when the material is undergoing strain hardening after yielding, piling-up of dislocation loops continues while the leading dislocation is impeded by the particle induced stress field. From Fig. 7e the force due to the cumulative pile-up reaches a critical point, which causes the leading dislocation to break out so a saturation plastic flow ensues. The looping action is now similar to the motion observed in the previous case when under an applied compressive stress.

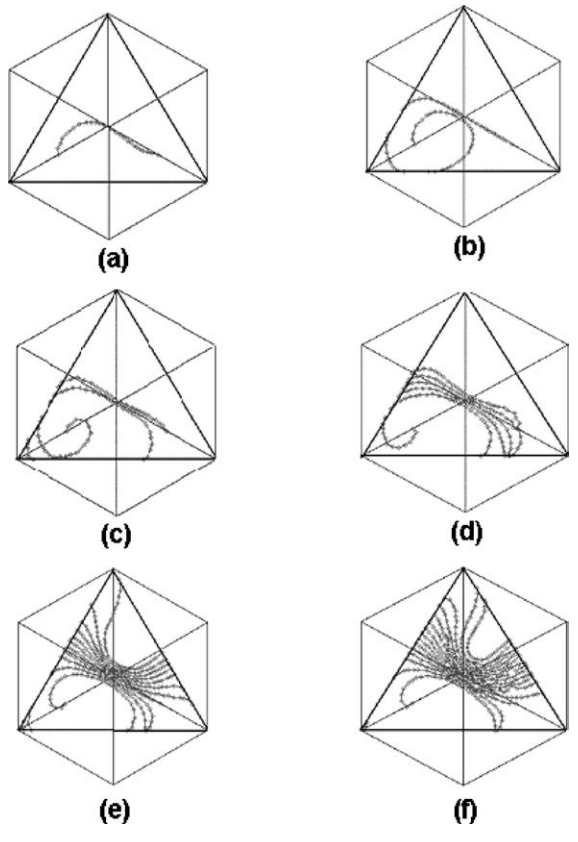

Figure 7 Dislocation configurations corresponding to points labeled on simulated stress-strain diagram (Fig. 6) for the crystal with an embedded particle. The figure shows dislocation configurations (a) at the beginning of elastic deformation in compression; (b) at the beginning of plastic deformation in compression; (c) just after the beginning of plastic deformation in compression; (d) after generation of several dislocation loops while still experiencing strain hardening; (e) at the beginning of the saturation of plastic flow in compression; and (f) at the strain reversal point of -0.0025 strain.

The configuration at the end of compressive loading, shown in Fig. 7f, is almost identical to that at the end of compressive loading for the previous tension-first case, Fig. 5f.

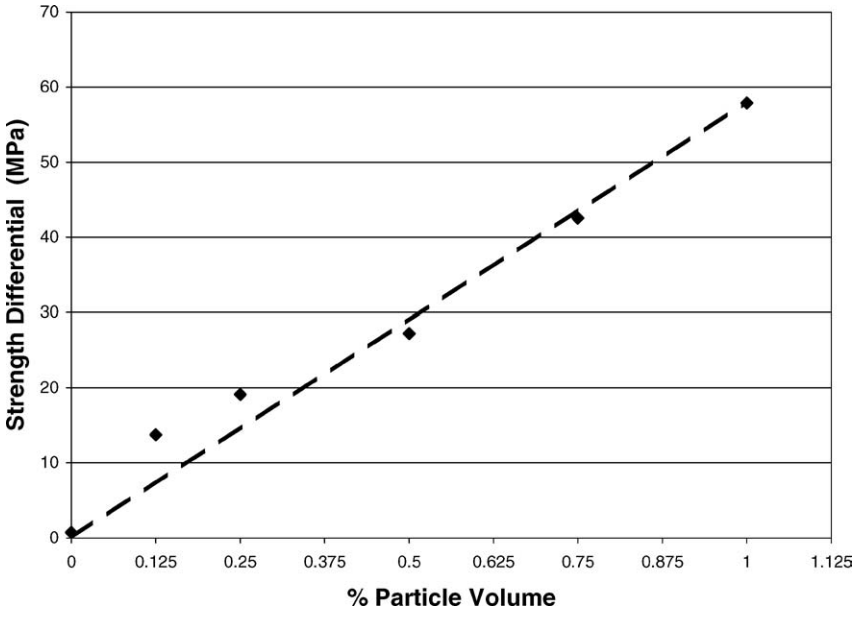

Figure 8 Strength differential ($\Delta\sigma_y = \sigma_y^t - \sigma_y^c$) caused by misfit particle as a function of normalized particle volume (the value of unity represents a particle with radius 2,000 b).

3.2. Effect of particle size

One can define the strength differential within the present context, $\Delta\sigma_y$, similar to the case in Equation 3, as

$$\Delta\sigma_y = \sigma_y^t - \sigma_y^c, \tag{14}$$

where σ_y^t and σ_y^c are the magnitudes of tensile and compressive flow stresses (both are positive quantities), respectively, obtained from the DD simulation. The strength differential caused by the misfit particle of radius 2,000 b is 58 MPa. Calculations of various particle radii were also carried out to examine the effect of particle size. All other simulation parameters remained unchanged. Fig. 8 shows the variation of strength differential as a function of particle volume. The particle volume in the figure is normalized by that of the 2,000 b-radius particle. The relationship is approximately linear. Owing to the model setup, a smaller particle means that the prescribed slip plane is at a greater distance from the particle edge, and thus a weaker local stress field is interfering with the dislocation glide.

3.3. Effect of strain rate

The simulation results presented thus far are based on an applied strain rate of 0.1 s^{-1}. The effect of strain rate is examined by carrying out calculations using two additional magnitudes: 1.0 and 10 s^{-1}. In the cases where no particle exists, the magnitudes of tensile and compressive flow stresses are equivalent for a given strain rate (i.e., $\Delta\sigma_y = 0$). The flow stress values for the pure matrix are 52, 53 and 83 MPa for the strain rates of 0.1, 1.0 and 10 s^{-1}, respectively. The flow stress increases with strain rate, although the difference between the cases of 0.1 and 1.0 s^{-1} is small. Fig. 9 shows the strain rate effect for the material containing a particle

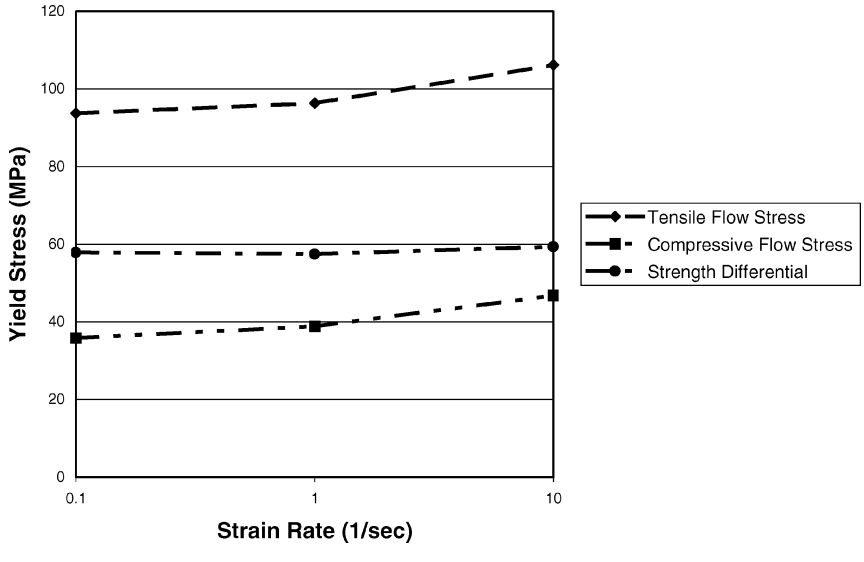

Figure 9 Strain rate effect for the crystal containing a particle with a radius of 2,000 b and a volumetric misfit of 3%.

of radius of 2,000 b. Here the quantities of tensile flow stress σ_y^t, compressive flow stress σ_y^c, and strength differential $\Delta\sigma_y$ are included in the same plot. It can be observed that, while strain-rate sensitivity of the flow stress is evident, the strength differential remains relatively unaffected by the applied strain rate. This can be explained by the fact that a higher strain rate results in a faster driven dislocation motion and therefore less efficient pile-up of loops for enhancing the bias in reversed yielding.

4. Discussion

While the present work is motivated by the Bauschinger effect for metals and alloys, the strength differential obtained from the DD simulation manifests itself in a different way. In the Bauschinger effect and the associated back stress concept, the yield strength during reversed loading is smaller than that in forward loading, regardless if the test is tension-first or compression-first. Here, the misfit elastic field results in a bias of flow stress toward one direction. This, of course, is because of the problem geometry that the glide plane is not intercepting the particle. There are two main reasons for setting up the problem as such. Firstly, as mentioned in the introduction, a given dislocation loop in a material of dilute particle concentration is expected to sweep a large area in the matrix before encountering a particle head-on. Therefore we devote our attention to the interaction between dislocations and the misfit elastic field that exists throughout the matrix. Secondly, to capture Orowan looping of dislocations around the particle and therefore to investigate the physical nature of the *commonly perceived* "back stress", one will need to include the image stress effect in the simulation. It turns out that incorporating image stresses in a rigorous way is an extremely difficult task even for the simplest dislocation and particle geometries. There have been very specialized (and not necessarily closed-form) solutions reported for some dislocation-particle interaction problems [28, 29]. Attempts have also been made on utilizing DD simulation to capture salient features of the image stress effect for the special case of a circular dislocation loop pile-up surrounding a short rigid fiber [22]. Nevertheless, the current study does not include any image stress in the simulations. It is felt that the effect of image stress is small because the main action of image stress from a stiff particle is to retard the motion of oncoming colliding dislocations and in the present case the closest distance between the slip plane and the particle edge is greater than 40% of the particle radius.

To test our assumption, calculations are carried out setting the elastic constants of the particle the same as those of the matrix (while keeping the misfit and other loading and geometric conditions identical to the standard case in Section 3). The results are shown in Fig. 10a and b, where the tension-first and compression-first loading, respectively, are presented. In both cases the tensile plastic flow stress is about 80 MPa and compressive plastic flow stress is about 37 MPa. It is apparent, by comparing Fig. 10 with Figs 4 and 6, that the absolute flow stress values and the strength differential are only mildly affected. This is a manifest that the effect of image stress will not contribute much in the present situation. The dislocation behavior is dominated by the particle misfit field.

Since the combination of various forms of dislocation-particle and dislocation-dislocation interactions always takes place in actual experiments, the sole effect of the misfit elastic field, as presently investigated, can only be studied by theoretical means. Our results nevertheless illustrate the possible contribution to strength differential originating from the misfit field. This work focuses on the baseline that there is a single initial dislocation source in a specified slip plane and that a single particle exists in the crystal. The particular geometric relationship between the dislocation source and the particle chosen in this study also affects the simulation outcome. As a consequence, care should be taken in arbitrarily generalizing the present results to actual crystal systems. Nevertheless, extension to multiple particles and multiple dislocation sources within the present simulation framework can be achieved in a straightforward manner to examine the effect of size, spatial distribution and volume fraction of particles on the strength differential and cyclic response in general. This will be left as future work. It is worth mentioning, at this juncture, that we have recently undertaken DD simulations of *monotonic* loading of a crystal containing multiple particles [30].

While a clear strength differential was found in the current study, the results shown in Figs 4 and 6 suggest that the conceptual model in terms of Equations 1 and 2 does not apply in the present case. This is because it is not possible to identify a single back stress value, σ_B, in Equations 1 and 2 to describe the cyclic stress-strain response, which involves net strengthening as discussed above. Here, we propose the following modification to describe our simulation results,

$$\sigma_y^t = \sigma_0 + \sigma_{ps} + \sigma_B, \tag{15}$$

and

$$\sigma_y^c = \sigma_0 + \sigma_{ps} - \sigma_B, \tag{16}$$

where the subscript in σ_{ps} stands for "particle strengthening." Taking σ_0 as 52 MPa (from Fig. 2, the plastic flow stress without particle) along with $\sigma_y^t = 94$ MPa and $\sigma_y^c = 36$ MPa for the particle with radius 2,000 b (or, particle volume fraction 3.35%), it is obtained that $\sigma_{ps} = 13.0$ MPa and $\sigma_B = 29.0$ MPa. Utilizing particle volume fraction as a measure and applying linear interpolation, the net particle strengthening stress and back stress are enhanced by about 3.8 and 8.7 MPa, respectively, for every 1% increase in particle concentration. Although our computational model is an idealized special case, the net particle strengthening effect is not at much variance with experimental measurements on 6013 aluminum alloys containing silicon carbide particles [31], which showed an increase in yield strength of about 3.5 MPa per 1% particle volume fraction. Experimental information on misfit particle induced back stress is not readily available.

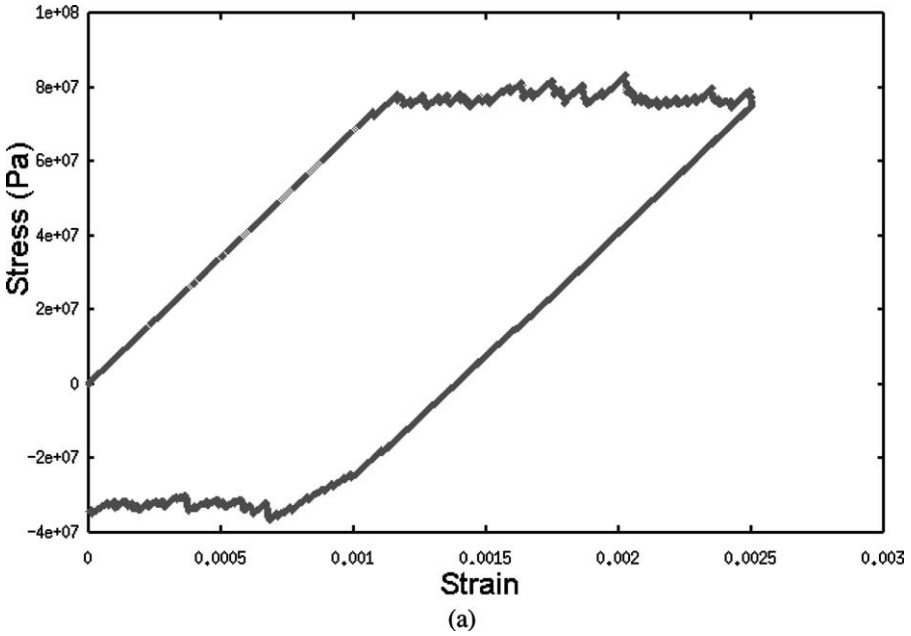

(a)

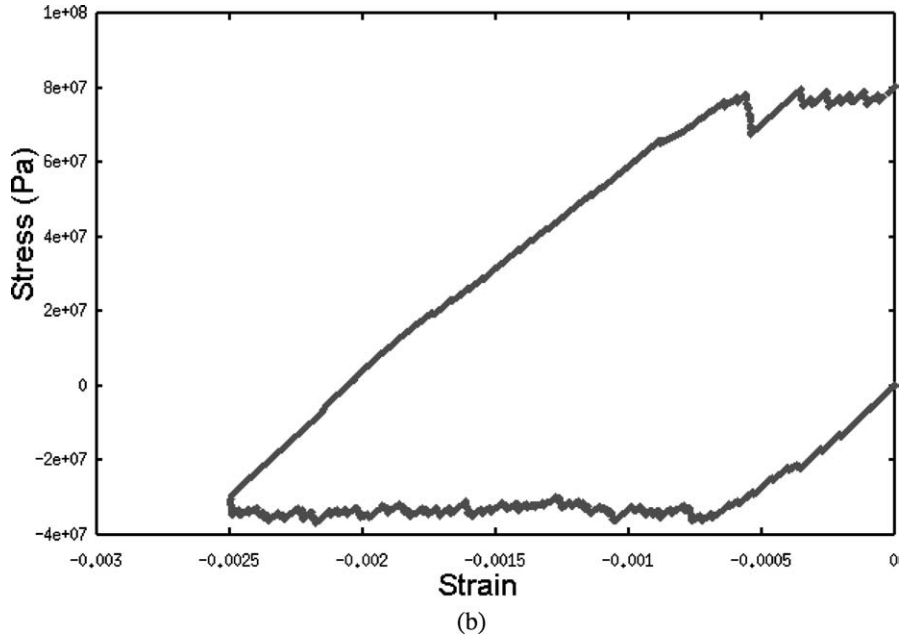

(b)

Figure 10 Simulated uniaxial stress-strain response of the crystal with an embedded particle of radius 2,000 b. The Burgers vector of the gliding dislocation is $\frac{b}{\sqrt{2}}[10\bar{1}]$. The strain rate is 0.1 s^{-1}. (a) Tension-first loading; (b) compression-first loading.

As depicted in Fig. 1, the initial Frank-Read source is not at a symmetric location with respect to the particle (i.e., it is biased toward one side away from the particle edge), so a concern may arise that the strength differential may be a natural consequence of this geometric bias. To test this we undertake a simulation involving a second Frank-Read source lying in another (111) plane as shown in Fig. 11a. The two (111) planes are symmetric about the particle and the two Frank-Read sources are geometrically arranged such that the center of particle is the "inversion center" of the two dislocations before and during deformation. The particle radius is 2,000 b and the tension-first loading has an applied strain rate of 0.1 s^{-1}. All other parameters remain the same. If no particle exists, the simulated stress-strain response was found to be essentially the same as in Fig. 2, implying minimal interaction of dislocations in the two slip planes, which are spaced quite far apart. Fig. 11b shows the stress-strain response of the crystal containing the particle. It is clear that the strength differential exists. The response appears essentially the same as in Fig. 4. As a consequence, the strength differential observed from the present simulation study is not an artifact of the problem setup.

Further tests are conducted using only one dislocation source. Again the case of Fig. 4 serves as a basis for comparison. Fig. 12 shows the stress-strain response using the same simulation parameters as in Fig. 4 except that the Burgers vector is now reversed (i.e., $\frac{b}{\sqrt{2}}[\bar{1}01]$). The similarity between the two figures is evident. Although the misfit field caused by the particle exerts a force on the dislocation in the opposite direction, the same applied load also tends to move the dislocation *in this opposite direction*. The net outcome

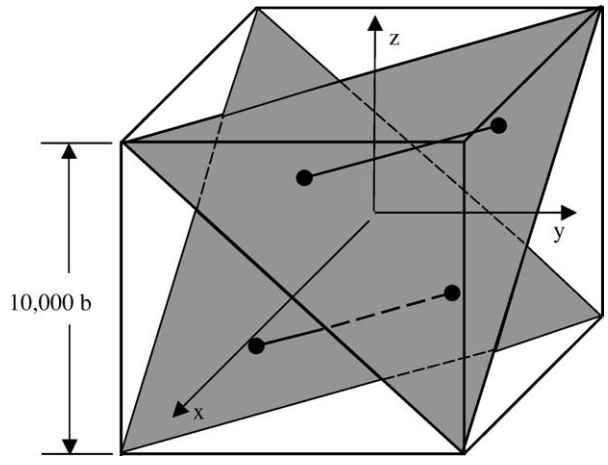

(a)

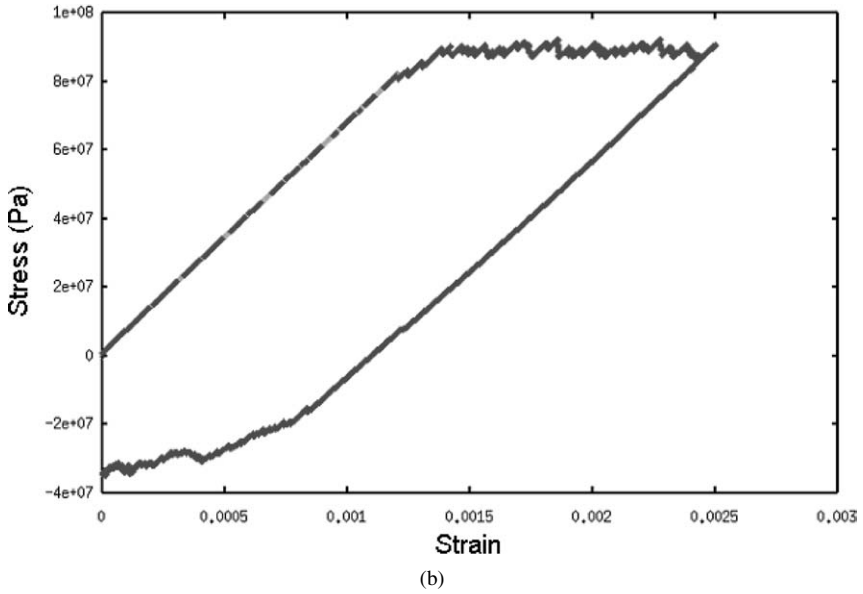

(b)

Figure 11 (a) Schematic of the problem geometry with two Frank-Read dislocation sources on (111) planes that are symmetric about the particle. The origin is set at the center of the cube (and the particle of radius 2000 b). The dislocation sources are both parallel to the $[\bar{1}10]$ direction. One source has two end nodes pinned at the coordinates of $x = 1667\,b$, $y = -3333\,b$, $z = -3333\,b$ and $x = -3333\,b$, $y = 1667\,b$, $z = -3333\,b$, with a Burgers vector of $\frac{b}{\sqrt{2}}[10\bar{1}]$. The other source has two end nodes pinned at the coordinates of $x = 3333\,b$, $y = -1667\,b$, $z = 3333\,b$ and $x = -1667\,b$, $y = 3333\,b$, $z = 3333\,b$, with a Burgers vector of $\frac{b}{\sqrt{2}}[\bar{1}01]$. (b) Simulated uniaxial stress-strain response of the model depicted in (a).

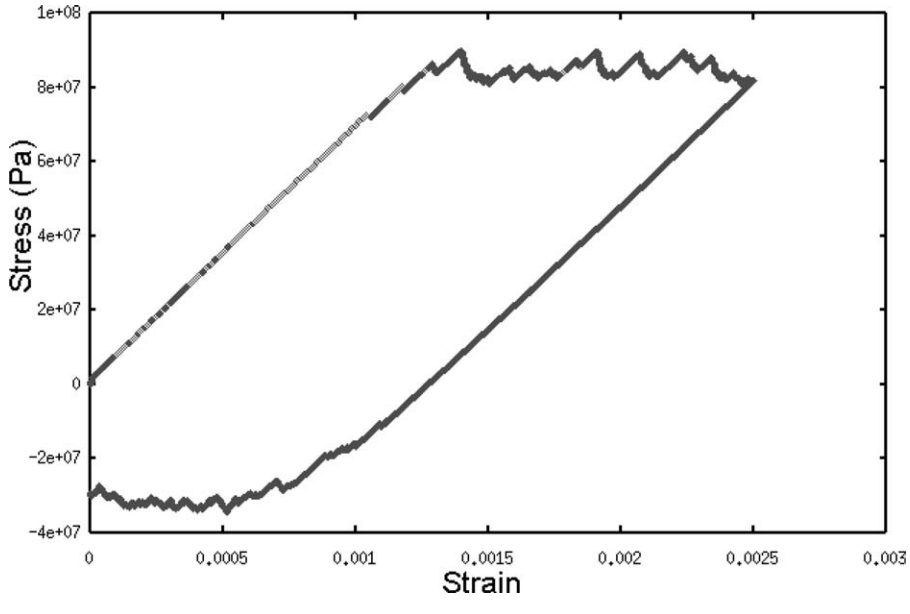

Figure 12 Simulated uniaxial stress-strain response of the crystal with an embedded particle of radius 2,000 b. The Burgers vector of the gliding dislocation is $\frac{b}{\sqrt{2}}[\bar{1}01]$. The simulation consisted of tensile loading at a constant rate of 0.1 s^{-1} to an applied strain of 0.0025, followed by a load reversal at the same strain rate back to zero strain.

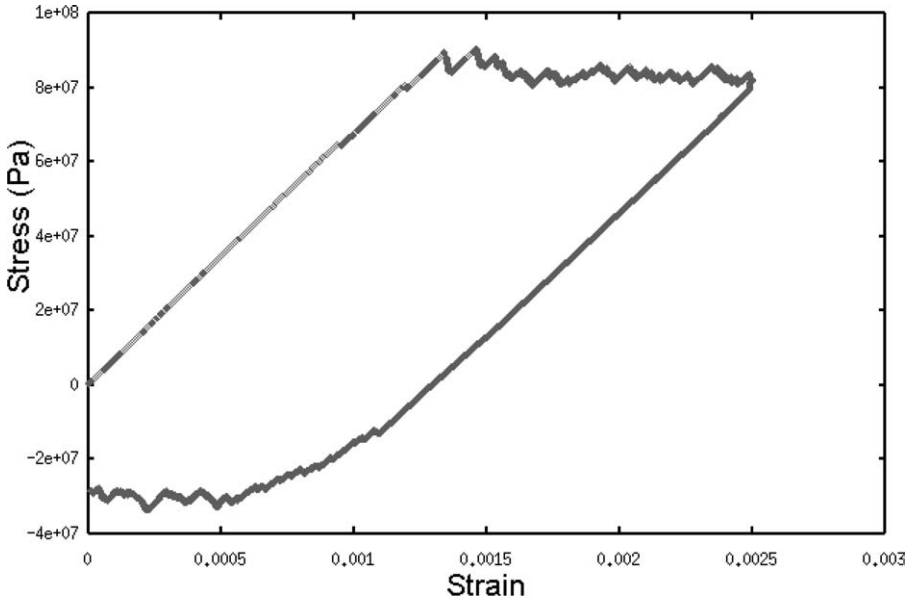

Figure 13 Simulated uniaxial stress-strain response of the crystal with an embedded particle of radius 2,000 b. The Burgers vector of the gliding dislocation is $\frac{b}{\sqrt{2}}[10\bar{1}]$. The simulation consisted of tensile loading at a constant rate of 0.1 s^{-1} to an applied strain of 0.0025, followed by a load reversal at the same strain rate back to zero strain. The dislocation source is placed at a symmetric location, with reference to the case of Fig. 4, with the two end points pinned at the coordinates of $x = 3333\ b$, $y = -1667\ b$, $z = 3333\ b$ and $x = -1667\ b$, $y = 3333\ b$, $z = 3333\ b$.

is that the same type of bias in flow stress exists for the two cases (Figs 4 and 12). When the single dislocation source is placed at the symmetric location (see Fig. 11a, but with only one source with Burgers vector $\frac{b}{\sqrt{2}}[10\bar{1}]$ in the upper (111) plane), essentially the same kind of strength differential results, Fig. 13. This is easily understood, again due to the fact that both the particle stress field and applied stress field tend to promote dislocation glide *in the same direction*.

5. Conclusions

Micromechanical simulations of dislocation-particle interactions in a crystal containing a misfit particle were performed using dislocation dynamics. Attention is focused on continuous forward and reversed loading and the associated macroscopic strength differential. It was found that, even when the slip plane does not intersect the particle, the misfit elastic stress field still interferes with the dislocation motion so pile-up of dislocation loops can develop. The formation of dislocation substructure in turn gives rise to strength differential. The plastic flow stress is higher in tension than in compression for the special problem configuration considered in this study. The misfit particle induced strength differential is independent of the loading sequence (tension-first vs. compression-first). The strength differential is not merely a shift in stress-strain response toward one direction because, as quantified in this study, there is also a net strengthening effect due to the particle. The effect of strength differential becomes larger with increasing particle size. While the overall response showed the typical strain rate hardening effect, the strength differential is largely unaffected by the applied strain rate. This fundamental study illustrates the possible contribution of dislocation-misfit particle interaction, other than the commonly recognized Orowan mechanism, to the buildup of back stress and the cyclic strength differential behavior in metals and alloys.

Acknowledgments

This work was supported by the Air Force Office of Scientific Research under Grant F49620-01-1-0565 (Program Manager Dr. Craig Hartley).

References

1. D. V. WILSON, *Acta Metall.* **13** (1965) 807.
2. A. ABEL and R. K. HAM, *ibid.* **14** (1966) 1489.
3. R. E. STOLTZ and R. M. N. PELLOUX, *Metall. Trans.* A **7A** (1976) 1295.
4. D. V. WILSON and P. S. BATE, *Acta Metall.* **36** (1986) 1107.
5. L. M. BROWN and W. M. STOBBS, *Philos. Mag.* **23** (1971) 1185.
6. *Idem.*, *ibid.* **23** (1971) 1201.
7. J. D. ATKINSON, L. M. BROWN and W. M. STOBBS, *ibid.* **30** (1974) 1247.
8. L. M. BROWN and D. R. CLARK, *Acta Metall.* **25** (1977) 563.
9. H. LILHOLT, *ibid.* **25** (1977) 571.
10. M. TAYA, K. E. LULAY, K. WAKASHIMA and D. J. LLOYD, *Mater. Sci. Engng.* A **124** (1990) 103.
11. S. SURESH, "Fatigue of Materials," 2nd ed., (Cambridge University Press, Cambridge, 1998) p. 100.
12. D. HULL and D. J. BACON, "Introduction to Dislocations," 3rd ed., (Pergammon Press, New York, 1984) p. 242.
13. C. TEODOSIU, "Elastic Models of Crystal Defects" (Springer-Verlag, New York, 1982).
14. L. P. KUBIN, G. CANOVA, M. CONDAT, B. DEVINCRE, V. PONTIKIS and Y. BRECHET, *Solid State Phenomena* **23/24** (1992) 455.
15. E. VAN DER GIESSEN and A. NEEDLEMAN, *Modeling Simul. Mater. Sci. Engng.* **3** (1995) 689.
16. B. DEVINCRE, in "Computer Simulations in Materials Science," edited by H. O. Kirchner *et al*. (Kluwer Academic Publishers, 1996) p. 309.
17. K. W. SCHWARTZ and F. K. LEGOUES, *Phys. Rev. Lett.* **79** (1997) 1877.
18. H. M. ZBIB, M. RHEE and J. P. HIRTH, *Int. J. Mech. Sci.* **40** (1998) 113.

19. M. RHEE, H. M. ZBIB, J. P. HIRTH, H. HUANG and T. DE LA RUBIA, *Modeling Simul. Mater. Sci. Engng.* **6** (1998) 467.
20. N. GHONIEM and L. Z. SUN, *Phys. Rev.* B **60** (1999) 128.
21. A. NEEDLEMAN, *Acta Mater.* **48** (2000) 105.
22. T. KHRAISHI and H. M. ZBIB, *Comput. Mater. Sci.* **24** (2002) 294.
23. *Idem.*, *J. Engng. Mater. Technol.* **124** (2002) 342.
24. T. A. KHRAISHI, H. M. ZBIB, T. D. DE LA RUBIA and M. VICTORIA, *Metall. Mater. Trans.* B **33** (2002) 285.
25. J. P. HIRTH and J. LOTHE, "Theory of Dislocations" (Krieger Publishing Company, 1982).
26. B. DEVINCRE, *Solid State Commun.* **93** (1995) 875.
27. M. RHEE, J. S. STOLKEN, V. V. BULATOV, T. D. DE LA RUBIA, H. M. ZBIB and J. P. HIRTH, *Mater. Sci. Engng.* A **309/310** (2001) 288.
28. J. DUNDERS, in "Recent Advances in Engineering Science," edited by A. C. Eringen (1965) Vol. 2, p. 223.
29. S. D. GAVAZZA and D. M. BARNETT, *Int. J. Engng. Sci.* **12** (1974) 1025.
30. T. A. KHRAISHI, L. YAN and Y.-L. SHEN, *Int. J. Plasticity* **20** (2004) 1039.
31. A. L. GEIGER and J. A. WALKER, *J. Metals* **43**(8) (1991) 8.

Received 5 August 2003
and accepted 3 March 2004